Modeling and Waveform Optimization of a Nano-motion Piezo Stage

Roel J. E. Merry, *Member, IEEE*, Martijn G. J. M. Maassen, Marinus (René) J. G. van de Molengraft, Nathan van de Wouw, *Member, IEEE*, and Maarten Steinbuch, *Senior Member, IEEE*

***Abstract*—Piezo actuators are used in high-precision systems that require nanometer accuracy. In this paper, we consider a nano-motion stage driven by a walking piezo actuator, which contains four bimorph piezo legs. We propose a (model-based) optimization method to derive waveforms that result in optimal driving properties of the walking piezo motor. A model of the stage and motor is developed incorporating the switching behavior of the drive legs, the contact deformation, and stick-slip effects between the legs and the stage. The friction-based driving principle of the motor is modeled using a set-valued friction model, resulting in a model in terms of differential-algebraic inclusions. For this model, we developed a dedicated numerical time-stepping solver. Experiments show a good model accuracy in both the drive direction and the perpendicular direction. The validated model is used in an optimization, resulting in waveforms with optimal driving properties of the stage at constant velocity. Besides the model-based optimization, also a direct experimental data-based waveform optimization is performed. Experiments with the optimized waveforms show that compared to existing sinusoidal and asymmetric waveforms in literature the driving properties can be significantly improved by the model-based waveforms and even further by the data-based waveforms.**

***Index Terms*—Dynamical modeling, input optimization, non-smooth dynamics, piezo actuators.**

I. Introduction

PIEZO actuators are used in high-precision systems that require nanometer accuracy due to their attractive properties, such as good reproducibility, high stiffness, and fast response. Stepping piezo actuators are able to drive nano-motion stages at constant velocities in the order of nanometers per second to millimeters per second. To obtain good positioning and tracking performance of the stages, a driving principle of the stepping piezo actuators with a continuous actuation and smooth transitions between the driving piezo legs is desired.

Manuscript received September 3, 2009; revised February 16, 2010; accepted April 8, 2010. Date of publication June 21, 2010; date of current version May 11, 2011. Recommended by Technical Editor J. Ueda. This work was supported by the SenterNovem/Point One under the Micro and Nano Motion Project.

R. J. E. Merry and M. G. J. M. Maassen were with the Department of Mechanical Engineering, Eindhoven University of Technology 5600 MB Eindhoven, The Netherlands. They are now with TMC, 5600 AS Eindhoven, The Netherlands (e-mail: r.j.e.merry@tue.nl; martijnmaassen@gmail.com).

M. (René) J. G. van de Molengraft, N. van de Wouw, and M. Steinbuch are with the Department of Mechanical Engineering, Eindhoven University of Technology, 5600 MB Eindhoven, The Netherlands (e-mail: m.j.g.v.d.molengraft@tue.nl; n.v.d.wouw@tue.nl; m.steinbuch@tue.nl).

Color versions of one or more of the figures in this paper are available online at http://ieeexplore.ieee.org.

Digital Object Identifier 10.1109/TMECH.2010.2050209

In this paper, we consider a nano-motion stage driven by a walking piezo actuator. The walking piezo actuator employs four bimorph piezo legs to drive the stage in pairs of two. The orbits of the drive legs are defined by the electric drive waveforms to the motor. With the currently used sinusoidal and asymmetric waveforms [1], no satisfactory driving properties are obtained; stick-slip effects and different leg velocities at the transfer between the driving pairs of legs limit the actuation of the piezo legs at a constant velocity and result in a nonsmooth stage behavior. To reduce the effect of these performance limiting factors [2], a model-based approach is followed to obtain new actuator driver software. In this paper, we develop a model of the nano-motion stage and walking piezo actuator, which is experimentally validated and used to derive new waveforms by means of optimization techniques.

The model of the nano-motion stage with the piezo motor includes the alternating nature of the walking movement of the piezo legs, the contact dynamics, and the stick-slip effects between the motor and the stage. Although the piezo legs contain some hysteresis, in most applications nearly linear operating conditions are selected [3]. Therefore, in this paper, hysteresis is not taken into account. An overview of models for contact dynamics for an ultrasonic piezo motor is given in [4]. The contact between the piezo legs and the drive strip of the nano-motion stage is modeled using a (one-sided) nonlinear contact stiffness. The driving principle of the walking piezo motor is based on friction. Therefore, accurate modeling of the friction between the stage and motor is important. In [5], three different friction models are compared for a friction drive piezo actuator. It is found that the variation of the friction force due to a variation in normal force should be taken into account. To model the friction force, which depends on the normal forces, and to properly model stiction, a set-valued friction model is used [6]–[8].

Numerical simulation of the dynamic model, including the set-valued friction model could be performed by smoothening of the set-valued nonlinearity, but this leads to (nonunique) approximations and stiff differential equations [9]. Event driven methods [10] are not favorable for our application since we split the model of the piezo-driven nano-motion stage in a model in the drive direction and a model in the perpendicular direction, of which simulation results at each time step have to be combined. Furthermore, the model results are compared to experimental data at an equidistant sampling grid. Since we are interested in the effect of friction on the global dynamics, but not in exact timing information of stick-slip transitions, we exploit time-stepping methods to perform numerical simulations with the dynamic model, including the set-valued friction model [9], [11].

Here, we formulate the model in terms of a differential-algebraic inclusion, for which we develop a dedicated time-stepping solver. The model and numerical solver can be used for the optimization of the waveforms to the piezo legs to optimize the legs orbit design.

In the literature, several algorithms have been described for waveform optimization. In [12], a computationally efficient real-time trajectory optimization technique is proposed. Optimal input signals are derived in [13] for systems in which part of the trajectory is chosen fixed. Although interesting, these methods are not adopted in this paper since, firstly, in our problem the optimization is performed offline and as a consequence computational efficiency is not really an issue, and, secondly, the input signals to be designed are completely free.

Waveforms for piezo devices have already been studied in literature. In [14], triangular, rectangular, and sinusoidal waveforms for an inchworm actuator are compared. The sinusoidal and triangular waveforms perform best. The period time and slopes of triangular driving waveforms are optimized for maximum velocity in [15]. In [16], possible trajectories for a walking micro-robot employing six bimorph piezo legs are described. However, no trajectory optimization for a specific goal is performed. In [17], iterative learning control of two parameters is applied to obtain a smooth stepping function for a piezo stepper with six legs. To the authors' best knowledge, no trajectory optimization for bimorph walking piezo motors has been described yet in literature. In our previous work [1], we proposed asymmetric waveforms, which improve the driving properties of the bimorph walking piezo motor. The optimized waveforms derived in this paper will be compared to these asymmetric waveforms.

To find the global optimum for the optimization cost functions as considered in this paper, which are nonlinear and non-convex in the optimization parameters, stochastic methods are preferred over nonlinear gradient-based methods. Since the success of such algorithms is problem dependent, genetic algorithms (GA) [18], [19], simulated annealing (SA) [20], and two algorithms of particle swarm optimization (PSO) [21]–[23] are tested. For each method, also a two-phase approach is used, i.e., the global optimization is followed by a local gradient-based optimization [24], [25].

The contributions of this paper are threefold. Firstly, a model of the nano-motion stage driven by the walking piezo actuator, including the switching behavior of the piezo actuator and the contact dynamics and stick-slip behavior between the piezo motor and the stage, is presented. Secondly, a dedicated time-stepping solver is developed for the derived model, which is described by a set of differential-algebraic inclusions. Finally, optimal waveforms are derived by means of a model-based and a data-based optimization.

This paper is organized as follows. In Section II, the experimental setup will be discussed in more detail. The model and time-stepping solver will be presented in Section III. The model identification and validation will be shown in Section IV. Section V contains the waveform optimizations. Finally, conclusions will be drawn in Section VI.

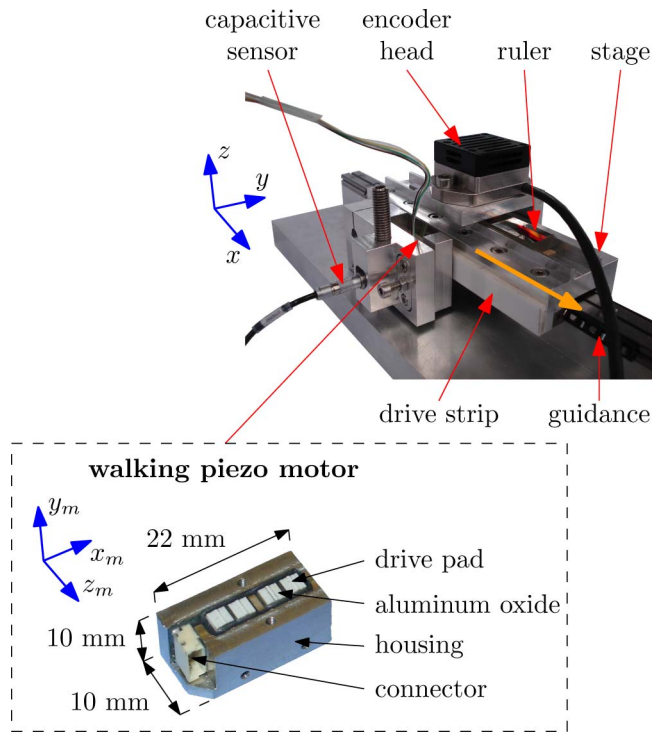

Fig. 1. Nano-motion stage driven by the walking piezo actuator.

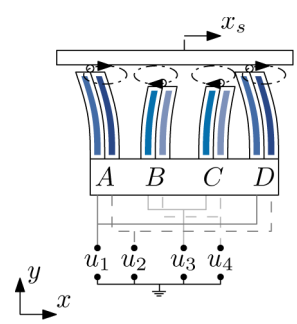

Fig. 2. Schematic working principle of the walking piezo motor. Only the driving electrode to the piezo stacks is shown, the ground electrodes on the individual stacks are omitted.

II. Experimental Setup

The one degree-of-freedom (DOF) nano-motion stage, as shown in Fig. 1, is equipped with a roller cage bearing to minimize the amount of friction in the stage movement. The position of the stage in x-direction is measured using a linear incremental encoder with a resolution of 0.64 nm. The displacement of the back of the motor housing is measured using a capacitive sensor with a resolution of 0.44 nm and a root-mean-square (rms) value of the noise of 1.6 nm. The motor is aligned with the drive strip of the stage using a dedicated motor suspension, as described in [1]. The drive pads of the piezo motor are pressed against the drive strip by two preload springs with a total preload force of 55 N.

The walking piezo motor contains four bimorph piezoelectric legs, which work together in pairs of two to drive the nano-motion stage, as shown in Fig. 2. Each leg contains two electrically separated piezo stacks. Each stack is driven by an electric

waveform $u_i(t)$ (V), $i \in \{1, 2, 3, 4\}$, which position the tips of the piezo legs in the (x_m, y_m)-plane (see Fig. 1). Applying equal voltages to the piezo stacks of one leg causes the leg to extend in y_m-direction. Different voltages introduce a bending of the leg in x_m-direction. The relative positions of the tips of the leg pairs 1 (legs A and D) and 2 (legs B and C) in x- and y-directions can be written as [2], [26]

$$\begin{aligned} x_{1,2} &= c_x(u_{1,3}(t) - u_{2,4}(t)) \\ y_{1,2} &= c_y(u_{1,3}(t) + u_{2,4}(t)) \end{aligned} \tag{1}$$

where c_x (m/V) and c_y (m/V) are the constant bending and extension coefficients, respectively.

The leg orbits are defined by choice of the waveforms $u_i(t)$ (V), $i \in \{1, 2, 3, 4\}$ in (1). Periodic alternating leg orbits are obtained with periodic waveforms [1]. Due to the preload, at least one pair of legs is in contact with the drive strip of the stage at all times.

The stage of Fig. 1 with the walking piezo actuator can track constant velocity set points ranging from nanometers per second to millimeters per second with an accuracy of nanometers to micrometers. Furthermore, point-to-point movement over 5 nm to the complete stroke of the stage can be made with a final static error below encoder resolution [1].

III. Modeling

This section contains the model of the walking piezo actuator and the nano-motion stage. First, the contact dynamics between the piezo legs and the stage are discussed, after which the models are presented. Since the model is described by a differential inclusion, we develop a dedicated time-stepping solver for the numerical simulations.

At low-stage velocities, the errors due to the shape of the input waveforms to the piezo motor are dominant over other errors, which are more evident at higher frequencies, e.g., due to measurement disturbances or system dynamics. Therefore, the model will be used for the waveform optimization at low-stage velocities, corresponding to low-drive frequencies of the piezo legs. The purpose of the model is to accurately describe the behavior of the system for frequencies $f < 50$ Hz, under the assumption that the stochastic disturbances and the high-frequency disturbances introduced by the hitting of the legs on the stage do not determine the performance. Also no fast dynamic effects are expected since the frequency range of interest is a factor ten below the first resonance frequency as present in the measured frequency response function (FRF) at 543 Hz (see Section IV and [1]).

Since the piezo legs are actuated in pairs by two input voltages as described in (1) and under the assumption that the legs in each pair are identical, each pair of legs can be lumped into a single leg. The leg positions are decomposed in orthogonal x- and y-displacements. Due to the decoupling of the x- and y-directions and the design of the motor suspension [1], the motor housing is assumed to move only in y-direction. Therefore, the model is split into two separate models for the x- and y-directions, respectively. This allows to compute the normal forces between the legs and the drive strip of the stage from the model in y-direction, which can then be used as an input for the model in x-direction to evaluate the friction forces between the legs and stage in x-direction.

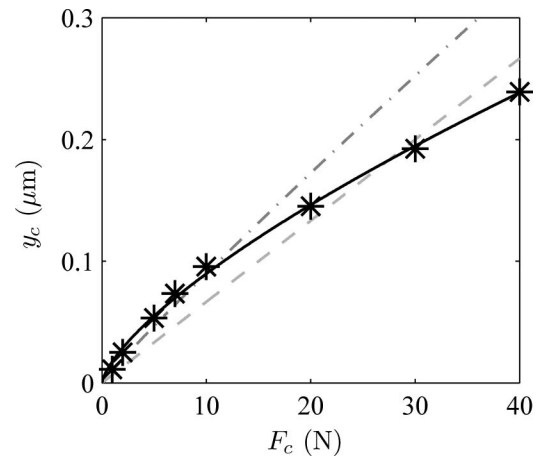

Fig. 3. Contact deformation, FEM model ($*$), Hertz contact (dark gray, dash-dotted), linear fit (light gray, dashed), and nonlinear fit (black, solid).

The voltage-actuated piezo legs are modeled as mass-spring-damper systems, analogous to existing piezo models [27]–[30]. In [2], we showed that the resonance frequencies of the piezo legs itself are located at frequencies $f > 215$ kHz, which is above the frequency range of interest for this model. The internal dynamics of the piezo legs can therefore be neglected. Since experiments show that the extensions of the different pairs of legs in (x, y)-directions are different and asymmetric, the static model of [2] and (1) is slightly extended by incorporating additional bending and extension coefficients as

$$\begin{aligned} x_1(t) &= c_{x_1} u_1(t) - c_{x_2} u_2(t) \\ y_1(t) &= c_{y_1} u_1(t) + c_{y_2} u_2(t) \\ x_2(t) &= c_{x_3} u_3(t) - c_{x_4} u_4(t) \\ y_2(t) &= c_{y_3} u_3(t) + c_{y_4} u_4(t) \end{aligned} \tag{2}$$

where x_1 and x_2 are, respectively, the x-positions of the first and second pair of legs and y_1 and y_2 are the corresponding positions of the leg models in y-direction.

A. Contact Dynamics

Due to the preload springs at least one pair of legs is in contact with the stage at all times. However, this contact is not rigid. The contact deformation is assumed to exist in y-direction only and is modeled by a spring with stiffness $k_{c_{1,2}}$, which may nonlinearly depend on the contact deformation. The static contact deformation obtained by a finite-element method (FEM) model of the aluminium oxide tip of piezo legs and aluminium oxide drive strip of the stage with physical dimensions is shown in Fig. 3. A Hertzian contact model for a cylinder on a flat surface [31], [32] equals

$$y_c = \frac{2F_c\lambda}{L}\left(1 + \ln\left(\frac{L^3}{2\lambda F_c R}\right)\right) \tag{3}$$

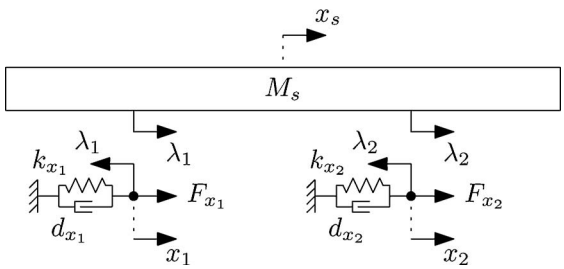

Fig. 4. Model of the system in x-direction.

where y_c (m) is the displacement, F_c (N) is the force, $L = 3$ mm is the contact length, $R = 0.2$ mm is the radius of the cylinder, and $\lambda = (1 - \nu^2)/\pi E$, with $\nu = 0.24$ the Poisson's ratio and $E = 377$ GPa the Young's modulus of the aluminium oxide material. The Hertzian contact model (3) resembles the contact deformation of the FEM model for contact forces $F_c < 10$ N, as shown in Fig. 3. Since the actual contact forces are larger, the Hertzian contact model is not applicable for this application. Also, a linear stiffness model is fitted through the FEM data, see Fig. 3, which does also not give satisfactory model accuracy. Therefore, the following nonlinear restoring force model

$$F_c = \left(\frac{y_c}{q_1}\right)^{1/q_2} \tag{4}$$

is fitted to the FEM data to obtain the parameter estimates $q_1 = 1.77 \times 10^{-8}$ and $q_2 = 0.705$.

The experimentally identified friction between the piezo legs and the stage in x-direction, obtained by measuring the angle at which the tilted stage with known mass starts sliding [31], showed a large variation, possibly due to the orientation of the contact surfaces between legs and motor at a microscopic level, environmental conditions or contamination of the sliding surfaces [4], [31]. Therefore, we confine ourselves to an elementary set-valued Coulomb friction model, which however does describe stick-slip phenomena

$$\lambda \in \mu F_N \operatorname{Sign}(v) \tag{5}$$

where μ is the friction coefficient, $F_{N_{1,2}}$ (N) is the normal force in the two pairs of piezo legs, v (m/s) is the relative sliding velocity between the sliding surfaces and the set-valued sign function is defined by

$$\operatorname{Sign}(x) = \begin{cases} \{-1\}, & \text{for } x < 0 \\ [-1, 1], & \text{for } x = 0 \\ \{1\}, & \text{for } x > 0 \end{cases} \tag{6}$$

Finally, experiments showed that the friction in the bearings is negligible.

B. Model x-Direction

The model for the x-direction is shown in Fig. 4. Since the mass of the piezo legs is very small compared to the mass of the stage, the legs are modeled as mass-less elements with stiffness $k_{x_{1,2}}$ (N/m) and damping $d_{x_{1,2}}$ (Ns/m). The subscripts $1, 2$ denote the leg pair. The force exerted by the piezo legs in x-direction due to the applied voltages to the stacks of the legs equals

$$\begin{aligned} F_{x_1} &= k_{x_1} x_1 = k_{x_1}(c_{x_1} u_1(t) - c_{x_2} u_2(t)) \\ F_{x_2} &= k_{x_2} x_2 = k_{x_2}(c_{x_3} u_3(t) - c_{x_4} u_4(t)) \end{aligned} \tag{7}$$

where we used (2).

In Fig. 4, the position of the stage is denoted by x_s (m) and the positions of the leg pairs by $x_{1,2}$ (m). Let the mass of the stage be represented by M_s (kg) and the friction forces between the pairs and the stage by $\lambda_{1,2}$ (N), which depend on the normal forces of the leg pairs in y-direction and are described by the set-valued friction model (5). The equations of motion for the model in x-direction incorporate the spring-damper model, reflecting the passive flexibility and dissipation properties of the legs, the applied forces $F_{x_{1,2}}$ due to the applied voltages as in (7) and the friction forces $\lambda_{1,2}$, and are given by the following differential inclusions

$$\begin{aligned} M_s \ddot{x}_s &= \lambda_1 + \lambda_2 \\ k_{x_1} x_1 + d_{x_1} \dot{x}_1 &= F_{x_1} - \lambda_1 \\ k_{x_2} x_2 + d_{x_2} \dot{x}_2 &= F_{x_2} - \lambda_2 \end{aligned} \tag{8}$$

where the friction forces $\lambda_{1,2}$ in (8) satisfy the following set-valued force laws:

$$\begin{aligned} \lambda_1 &\in \mu F_{N_1} \operatorname{Sign}(\dot{x}_1 - \dot{x}_s) \\ \lambda_2 &\in \mu F_{N_2} \operatorname{Sign}(\dot{x}_2 - \dot{x}_s) \end{aligned} \tag{9}$$

in which the set-valued sign function is defined by (6). The first equation of (8) describes the equation of motion for the stage and the latter two the equilibrium equations for the mass-less legs. The set-valued nature of the friction forces λ_1, λ_2 (9) between the leg, and the stage allows for a non-zero friction force at zero relative velocity. The latter fact implies that real sticking (zero relative velocity) is modeled.

C. Model y-Direction

A schematic representation of the system in y-direction is shown in Fig. 5(a). From top to bottom, the roller bearings are indicated by a spring k_b (N/m) and damper d_b (Ns/m). The contact dynamics are depicted as a nonlinear one-sided spring $k_{c_{1,2}}$ (N/m). The piezo legs are shown as spring-damper systems with spring $k_{y_{1,2}}$ (N/m) and damper $d_{y_{1,2}}$ (Ns/m). The motor housing is represented by the mass M_h (kg). Finally, the preload spring is denoted by k_p (N/m).

An FRF measurement in y-direction from the input voltages to the piezo legs to the measured displacement of the housing shows a purely static gain for frequencies $f < 500$ Hz. Since we require the model to be accurate up to a frequency of 50 Hz, inertial effects related to M_s are omitted in the model. Furthermore, since $k_b \gg k_{c_{1,2}}$, the stiffness of the bearing k_b is neglected in the model in y-direction. The compression of the preload springs due to the movement of the housing in y-direction is maximally 0.03% for a maximal motor displacement of 1 μm and a compression of the preload springs of 3 mm. The resulting variation in preload force is assumed to be negligibly small. Therefore, the preload springs are modeled as a constant

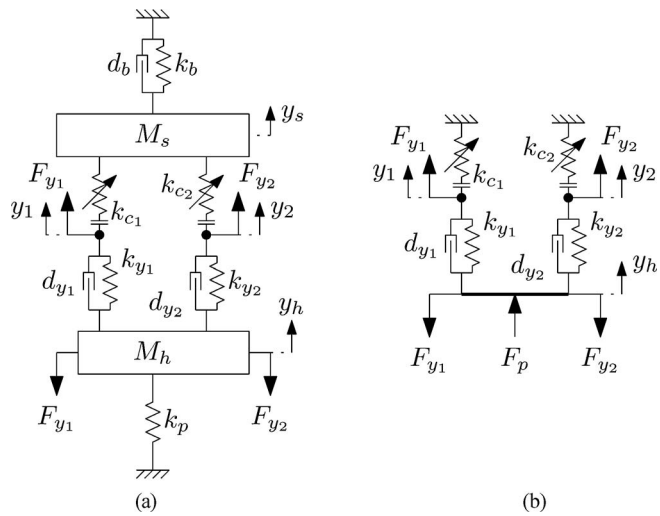

Fig. 5. Schematic representation and model of the system in y-direction. (a) Schematic representation. (b) Model y-direction.

preload force F_p. This leads to the model in y-direction, as shown in Fig. 5(b).

Using (2), the exerted forces by the piezo legs in y-direction due to the applied voltages equal

$$\begin{aligned} F_{y_1} &= k_{y_1} y_1 = k_{y_1}(c_{y_1} u_1(t) + c_{y_2} u_2(t)) \\ F_{y_2} &= k_{y_2} y_2 = k_{y_2}(c_{y_3} u_3(t) + c_{y_4} u_4(t)). \end{aligned} \tag{10}$$

The equations of motion of the model in y-direction are given by

$$\begin{aligned} k_{y_1}(y_h - y_1) + d_{y_1}(\dot{y}_h - \dot{y}_1) &= F_{c_1}(y_1) - F_{y_1} \\ k_{y_2}(y_h - y_2) + d_{y_2}(\dot{y}_h - \dot{y}_2) &= F_{c_2}(y_2) - F_{y_2} \end{aligned} \tag{11}$$

where the forces F_{y_1} and F_{y_2} exerted by the piezo legs due to the applied voltages follow from (10). The contact forces F_{c_1} and F_{c_2} are coupled through the motor housing and the constant given preload force F_p. Depending on the contact properties between the leg pairs and the stage, the preload force is divided over the contact forces $F_{c_{1,2}}$ of one or two leg pairs dependent on their elongation.

The preload force F_p is equal to the sum of the two contact forces $F_{c_{1,2}}$

$$F_p = F_{c_1}(y_1) + F_{c_2}(y_2). \tag{12}$$

The forces in the one-sided contact springs as function of the elongation of both leg pairs in y-direction can be calculated using (4) as

$$F_{c_{1,2}}(y_{1,2}) = \begin{cases} 2\left(\dfrac{y_{1,2}}{q_1}\right)^{1/q_2}, & \text{if } y_{1,2} \geq 0 \\ 0, & \text{if } y_{1,2} < 0. \end{cases} \tag{13}$$

The factor two is added since one leg in the model represents a pair of legs, i.e., $F_{c_{1,2}} = 2F_c$. The coupling between the models in x- and y-directions follow from the contact forces as $F_{N_{1,2}} = F_{c_{1,2}}$.

D. Numerical Methods

In this section, the methods used for the numerical simulations of the models in x- and y-directions are described. To facilitate the coupling between the models in x- and y-directions, fixed time solvers with a time step $\Delta t = 0.25$ ms are chosen for the simulations. The choice of the time step is a tradeoff between accuracy and calculation time of the simulation. Let the start of a time-step be denoted by t_A, then the end time equals $t_E = t_A + \Delta t$.

For the simulations in x-direction, the normal forces $F_{N_{1,2}}$ are required. Solvers for differential-algebraic equations can be used to simulate the model in y-direction [33], of which we omit a description for the sake of brevity. The obtained normal forces $F_{N_{1,2}}$ from the simulation in y-direction are subsequently used in the simulation of the model in x-direction.

The model in x-direction, described by (8) and (9), is in the form of a set of differential inclusions, which can be simulated using a time-stepping solver [11]. A dedicated time-stepping algorithm is developed to simulate the specific problem of Fig. 4, including the mass-less leg elements. Using a backward Euler discretization scheme for the time derivatives $\dot{x}_s$ and $\dot{x}_{1,2}$, the equations of motion (8) can be discretized as follows:

$$\begin{aligned} \dot{x}_{s,E} &= \dot{x}_{s,A} + \frac{(\lambda_1 + \lambda_2)\Delta t}{M_s} \\ x_{1,E} &= \frac{d_{x_1} x_{1,A} + (F_{x_1} - \lambda_1)\Delta t}{d_{x_1} + k_{x_1}\Delta t} \\ x_{2,E} &= \frac{d_{x_2} x_{2,A} + (F_{x_2} - \lambda_2)\Delta t}{d_{x_2} + k_{x_2}\Delta t} \\ x_{s,E} &= x_{s,A} + \dot{x}_{s,E}\Delta t \end{aligned} \tag{14}$$

where Δt is the fixed time-step and the subscripts $\cdot_A$ and $\cdot_E$ denote the values at the start and end times of the fixed step iteration, respectively. The discretized version of the friction law (9) is given by

$$\begin{aligned} \lambda_1 &\in \mu F_{N_1} \operatorname{sign}\left(\frac{x_{1,E} - x_{1,A}}{\Delta t} - \dot{x}_{s,E}\right) \\ \lambda_2 &\in \mu F_{N_2} \operatorname{sign}\left(\frac{x_{2,E} - x_{2,A}}{\Delta t} - \dot{x}_{s,E}\right). \end{aligned} \tag{15}$$

The iteration scheme for the dedicated time-stepping solver at each time-step is as follows.

1) Gather the known coordinates $x_{s,A}$, $\dot{x}_{s,A}$, $x_{1,A}$ and $x_{2,A}$, and actuator forces F_{x_1} and F_{x_2} at the beginning of each time instant, i.e., at time t_A.
2) Simulate the model in y-direction to retrieve the normal forces $F_{N_{1,2}}$ at the corresponding time instant.
3) Take the friction forces $\lambda_{1,2}$ from the previous time step as an initial estimate for the current time step.
4) Using a root finding algorithm, e.g., a fixed point iteration, compute the friction forces in the following iterative loop where the superscript K denotes the iteration number.
   a) Evaluate $x_{1,E}$, $x_{2,E}$, $x_{s,E}$, and $\dot{x}_{s,E}$ from (14) for given $\lambda_{1,2}$.

b) Update the friction forces $\lambda_{1,2}^{K+1}$ as

$$\lambda_1^{K+1} = \mathrm{prox}_{C_1}\left(\lambda_1^K + r\left(\frac{x_{1,E} - x_{1,A}}{\Delta t} - \dot{x}_{s,E}\right)\right)$$
$$\lambda_2^{K+1} = \mathrm{prox}_{C_2}\left(\lambda_2^K + r\left(\frac{x_{2,E} - x_{2,A}}{\Delta t} - \dot{x}_{s,E}\right)\right) \tag{16}$$

where $r > 0$, $C_i = [-\mu F_{N_i},\ \mu F_{N_i}]$, $i \in \{1, 2\}$, is the set of admissible friction forces and

$$\mathrm{prox}_{C_i}(x) = \begin{cases} -\mu F_{N_i} & \text{for } x \le -\mu F_{N_i} \\ x & \text{for } -\mu F_{N_i} < x < \mu F_{N_i} \\ \mu F_{N_i} & \text{for } x \ge \mu F_{N_i} \end{cases} \tag{17}$$

$i \in \{1, 2\}$, is the proximal point to the convex set C_i. Note that the proximal point formulation of the set-valued friction law in (16) is equivalent to that in (15) and is introduced to be able to compute λ_1, λ_2 by solving (16) using a root-finding algorithm.

c) If $\lambda_{1,2}^{K+1} - \lambda_{1,2}^K < \epsilon$ for a given desired accuracy ϵ, the simulation step is complete, otherwise continue to the next iteration at step 4a with the updated friction forces $\lambda_{1,2} = \lambda_{1,2}^{K+1}$.

In principle, the choice for $r > 0$ is free. The step size of the fixed point solver is determined by r. For small r the fixed point iteration is likely to converge but with low-convergence speed, whereas higher r speeds up the convergence. If r is chosen too large, the convergence of the scheme may be compromised (see also [9]). The choice for ϵ is a tradeoff between convergence speed of the fixed point iteration and accuracy of the determined friction forces.

IV. Experimental Validation

This section deals with the identification of the model parameters and subsequent validation of the identified models using experimental data.

A. Parameter Identification

For the parameter identification, it is assumed that the material properties for both leg pairs are identical. The constant parameters $P_f \in \{M_s, k_{x_{1,2}}, k_{y_{1,2}}, F_p, q_1, q_2\}$ are identified from separate experiments. Weighting the stage mass yields $M_s = 0.428$ kg. The parameters q_1 and q_2 are fitted to FEM data of the contact dynamics, as described in Section III-A. The stiffness of the pairs of legs in y-direction is determined as $k_{y_{1,2}} = EA/L = 3.2 \times 10^8$ N/m, where the cross area $A = 9$ mm^2, the length $L = 4$ mm, and the modulus of elasticity $E = 70$ GPa. The stiffness $k_{x_{1,2}}$ denotes a combined stiffness of the leg and motor suspension and is determined using the known mass M_s combined with the first resonance from the measured FRF in x-direction at 543 Hz, which yields $k_{x_{1,2}} = 5.0 \times 10^6$ N/m. The preload force $F_p = 55$ N.

The remaining damping parameters, the bending and extension coefficients of the legs, and the friction coefficient are determined using optimization techniques. For this purpose, experimental data obtained with the nano-motion stage at a fixed driving frequency of 10 Hz for differently shaped waveforms is used. The used waveforms are: 1) sinusoidal, 2) asymmetric [1], 3) rhombic waveforms (waveforms that lead to a tip trajectory with four linear sides of equal length) with 90° phase shift, and 4,5) two manually obtained alternatives of the asymmetric waveforms. The parameters $P \in \{d_{x_{1,2}}, d_{y_{1,2}}, c_{x_1}, c_{x_2}, c_{x_3}, c_{x_4}, c_{y_1}, c_{y_2}, c_{y_3}, c_{y_4}, \mu\}$ are obtained by solving the following minimization problem

TABLE I
Obtained Model Parameters Using PSO Optimization of (18)

Parameter	Unit	Value
$b_{y_{1,2}}$	Ns/m	$1.86 \cdot 10^6$
c_{y_1}	m/V	$1.49 \cdot 10^{-8}$
c_{y_2}	m/V	$1.87 \cdot 10^{-8}$
c_{y_3}	m/V	$1.33 \cdot 10^{-8}$
c_{y_4}	m/V	$1.38 \cdot 10^{-8}$
$b_{x_{1,2}}$	Ns/m	$2.98 \cdot 10^4$
c_{x_1}	m/V	$5.29 \cdot 10^{-8}$
c_{x_2}	m/V	$7.02 \cdot 10^{-8}$
c_{x_3}	m/V	$2.63 \cdot 10^{-8}$
c_{x_4}	m/V	$3.33 \cdot 10^{-8}$
μ	-	0.587

$$\min_P f(P) \tag{18}$$

with

$$f(P) = \sum_{i=1}^{5} \left\{\mathrm{rms}\left(\bar{r}_w - \hat{r}_w(P)\right) + \left|\left(\bar{r}_w(t_0) - \hat{r}_w(P, t_0)\right)\right|\right\} \tag{19}$$

where $\mathrm{rms}(\cdot)$ denotes the root-mean-square value, $|\cdot|$ the absolute value operator, and $w \in \{1, 2, 3, 4, 5\}$ the waveform number. Furthermore, $\bar{r}_w = \{\bar{x}_w, \bar{y}_w\}$ denotes the average experimental data over ten periods for each individual waveform number w and $\hat{r}_w(P) = \{\hat{x}_w(P), \hat{y}_w(P)\}$ reflects the model output. The averaging is performed to minimize the effect of stochastic disturbances. The second term in the objective function weights the start points in order to obtain an equal starting point for the steps of the model compared to the experimental data. Since the average values of the model and the experimental data are removed in every iteration due to the relative measurements, the second term also weights the end point of each step due to the periodicity.

The minimization problem (18) is performed using GA, SA, and PSO algorithms. The PSO algorithm [22], [23] appears to be best suitable for the identification problem at hand, i.e., with the PSO algorithm results the lowest objective function value $f(P)$ is obtained the most times for 200 runs of the optimization problem.

Since the results of the model in y-direction are required for the model in x-direction, first the identification is performed in y-direction after which the x-direction is identified. The identified model parameter values are given in Table I. When comparing the bending and extension coefficients of the different legs, it can be seen that the coefficients for the second pair are smaller than for the first pair, indicating that this pair makes

TABLE II
SIZES OF THE LEG TRAJECTORIES AND MODEL ERRORS OF THE DIFFERENT WAVEFORMS AT 10 HZ, WAVEFORMS 1–5 ARE USED FOR THE MODEL IDENTIFICATION AND WAVEFORMS 6–9 FOR THE MODEL VALIDATION

w	waveform type	stroke x (μm)	rms($\bar{e}_x$) (μm)	stroke y (μm)	rms($\bar{e}_y$) (μm)
1	sinusoidal	5.25	0.26	0.60	0.06
2	asymmetric [1]	3.92	0.19	0.40	0.04
3	rhombic 90 deg.	5.23	0.30	0.56	0.11
4	identification	1.52	0.11	0.81	0.06
5	identification	3.29	0.22	0.58	0.04
6	verification	3.04	0.22	0.71	0.05
7	verification	2.95	0.16	0.61	0.05
8	verification	1.84	0.13	0.65	0.06
9	rhombic 45 deg.	3.05	0.16	0.56	0.08

smaller steps. Different values are also obtained for the bending and extension coefficients within one pair as described by (2), indicating an asymmetric step shape.

The sizes of the leg trajectories as obtained with the different identification waveforms 1–5 in the experiments and in the simulations with the identified model are given in Table II. The model shows a good match with the experimentally obtained sizes of all waveform types.

B. Model Validation

The experimental results contain stochastic disturbances as well as disturbances caused by the roughness of the drive strip, contamination, etc. Therefore, the model response, obtained with the developed time-stepping solver of Section III-D, is compared to the experimental data of 200 periods for each waveform. The model errors are defined as $e_x = \bar{x} - \hat{x}$ and $e_y = \bar{y} - \hat{y}$, where $\bar{\cdot}$ denotes the average measurement over the different periods and $\hat{\cdot}$ the simulated model output. The data are offset to an average value equal to zero since only relative measurements are performed.

For the validation of the model, four additional waveforms, other than those used for the identification, are used. The waveforms numbered 6–8 are different, manually obtained variations of the asymmetric waveforms [1]. Waveform 9 is a rhombic waveform with 45° phase shift. Furthermore, the performance of waveforms 6 and 8 is validated for different drive frequencies $f \in \{5, 10, 20\}$ Hz, whereas the identification is performed only with a drive frequency $f = 10$ Hz.

The time responses of the model and experiments are compared for the asymmetric waveform $w = 7$ and rhombic waveform $w = 9$, shown in Fig. 6. The model and experimental results for the manually obtained alternative asymmetric waveform $w = 7$ are contained in Fig. 7. It can be seen that the model response overlaps the experimental data of the 200 periods in both x- and y-directions. The mismatch between the measured position and the model position around $t = 0.09$ s is located at the takeover point, at which the model accuracy is somewhat limited due to the chosen friction and contact models. In y-direction, a large deviation in measured position data is visible, which is caused by the limited accuracy of the measurements with the capacitive sensor, which is very sensitive to orientation

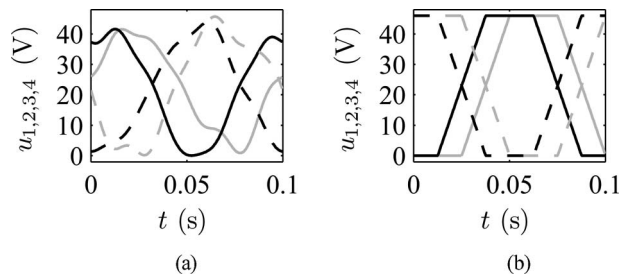

Fig. 6. Input voltages $u_i, i \in \{1, 2, 3, 4\}$ of the verification waveforms $w = 7$ and $w = 9$, u_1 (black, solid), u_2 (gray, solid), u_3 (black, dashed), u_4 (gray, dashed). (a) Validation waveform $w = 7$. (b) Rhombic waveform $w = 9$.

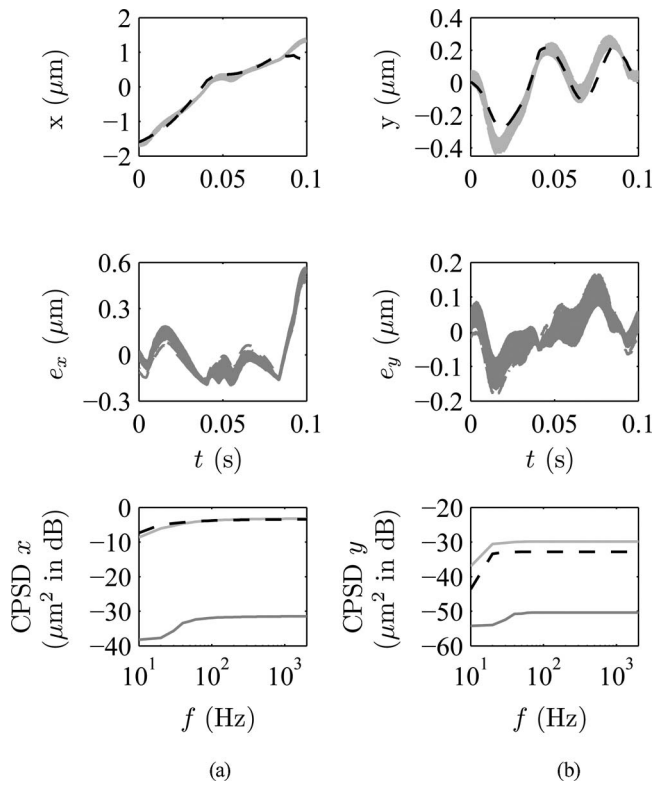

Fig. 7. Measured (solid, light-gray) and model (dashed, black) positions, errors (solid, dark gray) and CPSDs of the position and error signals in x- and y-directions for validation waveform $w = 7$. (a) x-direction. (b) y-direction.

errors and tilt of the motor housing. The cumulative power spectral densities (CPSDs) in the bottom figures show the accuracy of the model by the low CPSDs of the errors e_x and e_y. For frequencies $f \to \infty$, the CPSDs converge to the squared rms values of the signals.

The model also accurately describes the system response for non-harmonic waveforms such as rhombic waveforms ($w = 9$), as can be seen in Fig. 8. The CPSDs in the bottom figures of Fig. 8 show no increase in the errors at frequencies $f > 50$ Hz, so above the drive frequency of the experiments with which the model is identified. This confirms the assumption that the system performance is not determined by high-frequency disturbances.

The rms values of the errors in x- and y-directions for all identification and validation waveforms are shown in Fig. 9. The variation in the rms error over all 200 periods is also shown.

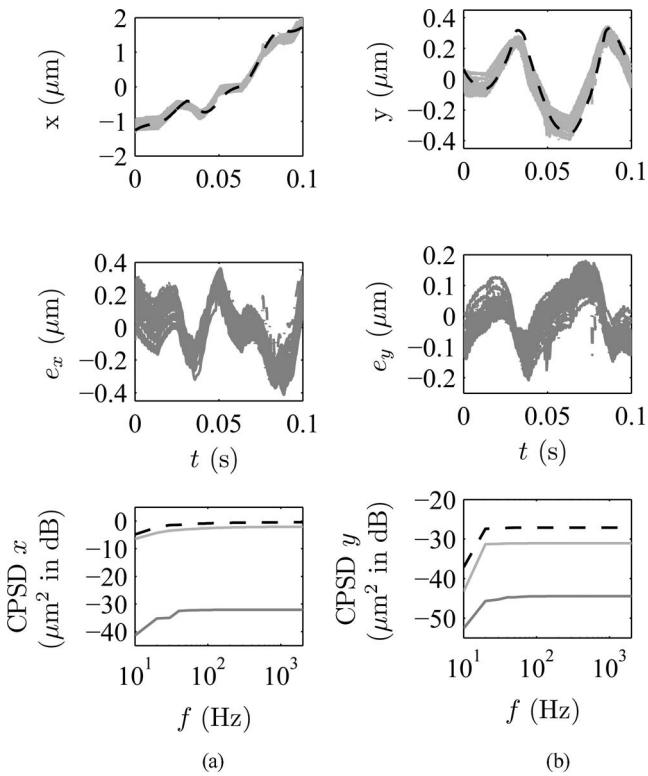

Fig. 8. Measured (solid, light-gray) and model (dashed, black) positions, errors (solid, dark-gray) and CPSDs of the position and error signals in x- and y-directions for validation waveform $w = 9$. (a) x-direction. (b) y-direction.

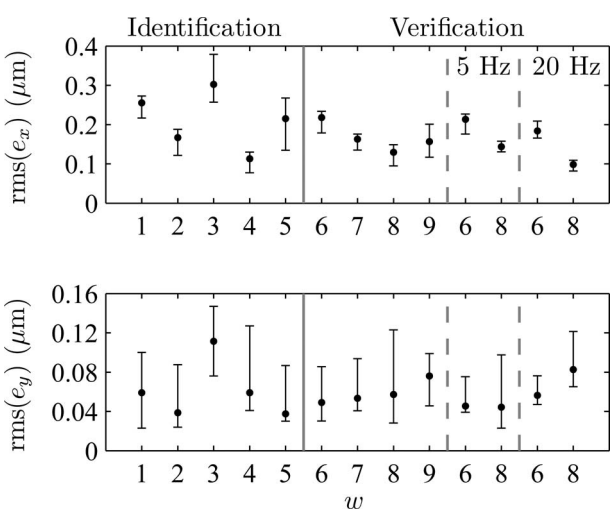

Fig. 9. Model errors e_x (μm) and e_y (μm) for various identification and verification waveforms with waveform driving frequencies $f_\alpha \in \{5, 10, 20\}$ Hz.

The average rms errors and sizes of the leg trajectories for the different waveforms are contained in Table II for a driving frequency of 10 Hz. The model describes the experimental data for all waveforms with an accuracy of 93% in x-direction and with an accuracy of 80% in y-direction. Note that the reduced model accuracy in y-direction is present for all identification and validation waveforms. Fig. 9 also shows that the model describes the experimental data obtained at drive frequencies $f \in \{5, 20\}$ Hz with the same accuracy. The model accuracy is approximately equal for the identification and validation waveforms. This is because the used validation waveforms show a large correlation with some of the identification waveforms. The verification waveforms $w = \{6, 7, 8\}$ are similar to the identification waveforms $w = \{4, 5\}$ in the sense that all are described by fourth-order Fourier series. Furthermore, the validation waveform $w = 9$ and the identification waveform $w = 3$ are both rhombic waveforms, but with a different phase.

With all waveforms (sinusoidal, asymmetric, rhombic, and manual waveforms used for the model identification and validation) stick-slip effects between the piezo legs and the stage are observed in the simulation results. Since slip between the legs and the drive surface of the stage affects the stage velocity and determines the quality of the waveforms to achieve the desired performance, it is important to include stick-slip in the model used for the waveform optimization.

V. Waveform Optimization

The model derived in Section IV can be used to optimize the waveforms for driving the walking piezo motor with different objective functions such as minimal energy, minimal driving frequency, maximum step size. In this research, we focus on optimizing the shape of the tip trajectories through the input waveforms to obtain a constant stage velocity. First, a model-based waveform optimization will be discussed, followed by a data-based experimental waveform optimization. The (dis)advantages of both methods are shown by means of experiments. The chosen reference velocity for the waveform optimization equals $\dot{x}_r = 50$ μm/s, which is chosen such that the required nominal drive frequency to achieve the reference velocity with asymmetric waveforms [1] is in the frequency range where the model is accurate.

A. Model-Based Waveform Optimization

The shape of the waveforms u_i (V), $i \in \{1, 2, 3, 4\}$ is chosen to be specified by eight equidistant points on one period $\alpha \in [0, 2\pi]$ rad. The optimization parameters ξ contain these eight points of each waveform that has to be optimized. Specifying each individual waveform u_i, $i \in \{1, 2, 3, 4\}$ by eight separate points would require $\xi = 32$ waveform parameters to be optimized. By adding dependencies between the waveforms, this number can be reduced at the cost of less freedom in the optimization.

From the optimization parameters ξ_i, $i \in \{1, 2, 3, 4\}$, of each waveform, the input voltages to the stacks are obtained by fitting a Fourier series model of order $n = 4$ in a least squares sense through the optimized points on one period described by ξ_i as

$$\{a^*_{k,i}, b^*_{k,i}\} = \arg \min_{a_{k,i}, b_{k,i}} (\xi_i - \hat{u}(\alpha, a_{k,i}, b_{k,i})) \tag{20}$$

where $a_{k,i}$ and $b_{k,i}$ are the Fourier coefficients and the Fourier series model

$$\hat{u}(\alpha, a_{k,i}, b_{k,i}) = \sum_{k=0}^{n} a_{k,i} \cos(k\alpha) + b_{k,i} \sin(k\alpha). \tag{21}$$

The waveforms u_i, $i \in \{1, 2, 3, 4\}$ for each iteration of the optimization now follow from (21) with the fitted Fourier coefficients $a^*_{k,i}$ and $b^*_{k,i}$, i.e., $u_i(\alpha) = \hat{u}(\alpha, a^*_{k,i}, b^*_{k,i})$. The Fourier series model is chosen because the waveforms should describe periodic signals and since the frequency content is limited, thereby avoiding excitation of high-frequency dynamics. By changing the shapes of the waveforms, the leg orbits change and thus the drive properties of the motor.

One might argue that direct optimization of the Fourier coefficients, i.e., $\xi_i = \{a_{k,i}, b_{k,i}\}$ would give the same results. Although direct optimization of the Fourier coefficients is possible and both sets of optimization parameters ξ_i could describe the same waveforms, different optimization problems are solved. The two sets of optimization points ξ_1 and ξ_2 of waveforms u_1 and u_2 directly describe eight points on the leg orbits of leg pair 1 as described by (1). A change of one of the eight points on the waveforms directly influences the optimized leg orbit. This direct relation of the optimization parameters to the leg orbits is not present when optimizing the Fourier coefficients $a_{k,i}, b_{k,i}$ since a change of one of these parameters changes a harmonic component in the waveform throughout the complete period of the waveform and thus on the complete leg orbit.

The goal of the optimization is twofold, namely, to design waveforms that, firstly, are able to accurately drive the stage at a given reference velocity and, secondly, minimize slip between the legs and stage to prevent wear of the drive surfaces and to optimize the efficiency of the actuator. Intuitively, one would choose the velocity error between the reference velocity and the obtained stage velocity of the model, i.e., $e_v = \dot{x}_r - \dot{x}_s$, to be minimized in the waveform optimization. This would however only address the first criterion and may lead to waveforms introducing extensive amounts of slip. Therefore, we opt for an objective function incorporating the leg velocities. The difference between the velocity of the legs and the reference velocity is minimized when the legs are in proximity of the stage. The desired clearance between the legs and the drive strip at which the relative velocity between legs and stage should be zero is denoted by δy, where $\delta y = 0$ denotes the model-based contact point and $\delta y < 0$ denotes an open distance between the legs and the drive strip. Note that by minimizing the occurrence of slip by optimizing the legs velocities when they are close to or in contact with the stage, we are effectively optimizing for the stage velocity as well.

Let the amplitudes of the points on the waveforms be contained in ξ. The optimization problem can now be formulated as

$$\min_{\xi} g(\xi) \tag{22}$$

with

$$g(\xi) = \mathrm{rms}(\dot{x}_r - \dot{x}^*_1(\xi)) + \mathrm{rms}(\dot{x}_r - \dot{x}^*_2(\xi)) \tag{23}$$

where the weighted leg velocities based on the desired clearance δy equal

$$\dot{x}^*_{1,2}(\xi) = \begin{cases} \dot{x}_{1,2}(\xi), & \text{if } y_{1,2} \geq \delta y \\ 0, & \text{if } y_{1,2} < \delta y. \end{cases} \tag{24}$$

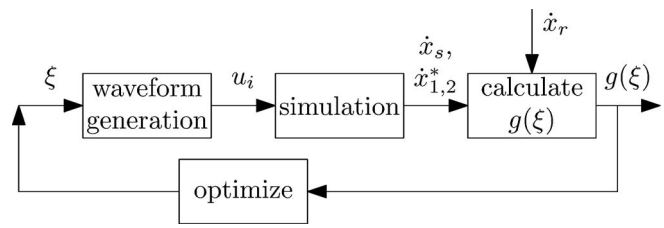

Fig. 10. Calculation objective function.

If the leg positions $y_{1,2} < 0$, the specific legs are not in contact with the stage. Note that slip is only implicitly minimized by (22). Slip could be minimized by extending the objective function (23), e.g., by the error between the individual leg velocities in the proximity of the stage.

The objective function for each iteration in the optimization is schematically shown in Fig. 10. For the waveform optimization of (22) also GA, SA, and PSO algorithms are tested. For this problem, the lowest objective function value $g(\xi)$ is obtained the most times for 200 optimization runs using SA [20].

In the next section, the results for a model-based optimization with eight individual parameters per waveform, i.e., ξ contains 32 parameters, and a clearance of $\delta y = 0.05$ μm are shown. For this optimization, the driving frequency is chosen as the frequency required to drive the stage at a velocity of 50 μm/s with the asymmetric waveforms [1]. This leads to a driving frequency $f_\alpha = 14$ Hz.

B. Validation of New Waveforms

In this section, the results of the experiments with the waveforms obtained from the model-based optimization are presented. The optimal waveforms are shown in Fig. 11. It can be seen that the shapes of all waveforms are different. This indicates that the waveform optimization accounts for the differences in the piezo legs (see also Table I).

The velocity errors of the simulations and experiments, defined as $e_{v,s} = \dot{x}_r - \dot{x}_s$ and $e_{v,e} = \dot{x}_r - \dot{x}_e$, respectively, are shown in Fig. 11 for the model-based optimal waveforms. The velocity v_e is obtained from the experiment by numerical differentiation of the encoder output and a subsequent anti-causal filtering of the differentiated signal by a fifth-order low-pass filter with a cut-off frequency $f_c = 500$ Hz. It can be seen that the velocity obtained in simulation approximates the desired stage velocity of 50 μm/s better than the experimentally obtained velocity.

The rms values of the velocity errors equal $\mathrm{rms}(e_{v,s}) = 10.24$ μm/s and $\mathrm{rms}(e_{v,e}) = 25.14$ μm/s (note that the reference velocity is 50 μm/s). The cumulative PSDs of the velocity errors show the difference between simulation and experiment, which is caused by the model error. The model mismatch is influenced by the contact dynamics and friction model, both of which could only be identified with limited accuracy due to the sensitivity of the capacitive sensor in the current setup. The influences of even small model errors become more apparent in the velocity signals.

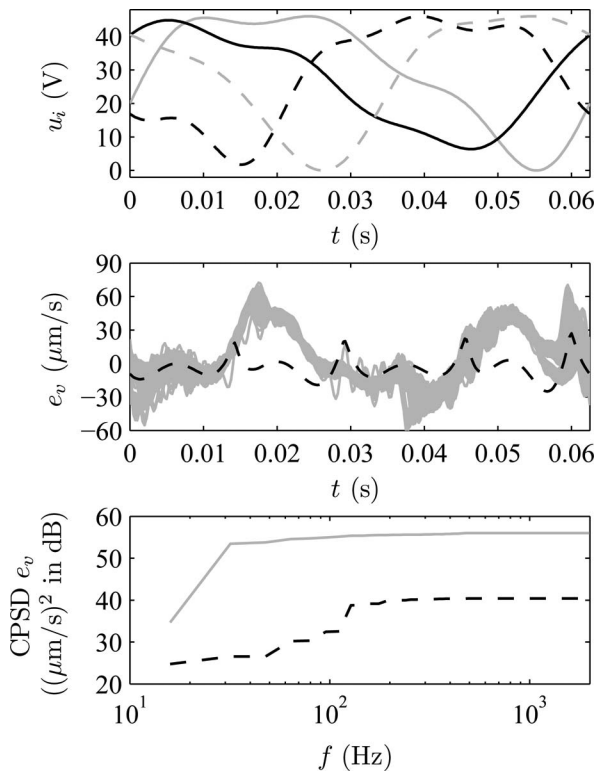

Fig. 11. Waveforms, velocity errors obtained with the model (black, dashed) and experiments (solid, gray) and cumulative PSDs of the errors for the model-based optimization.

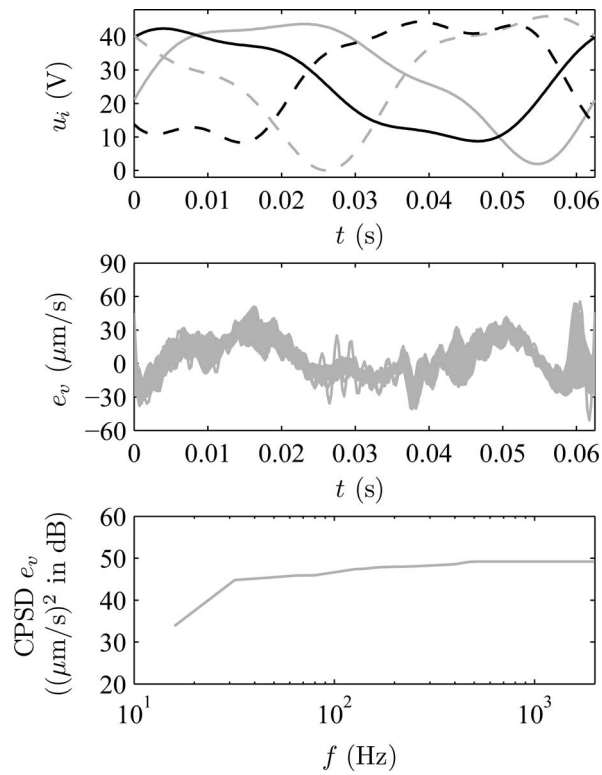

Fig. 12. Waveforms, velocity errors and cumulative PSD of the error for the data-based optimized waveforms.

C. Data-Based Waveform Optimization

To eliminate the influence of the model mismatch, also a data-based experimental waveform optimization is performed. For this purpose, the simulation in the calculation of the objective function (see also Fig. 10) is replaced by an experiment with the nano-motion stage and walking piezo leg actuator. For the data-based waveform optimization, the leg velocities cannot be measured. Therefore, for the data-based waveform optimization, the velocity error between reference and stage is minimized, resulting in the following data-based objective function for the optimization problem (22):

$$g(\xi) = \mathrm{rms}(\dot{x}_r - \dot{x}_{s,e}(\xi)). \tag{25}$$

The sampling frequency for the experiments equals 4 kHz.

The obtained waveforms of the data-based optimization are shown in Fig. 12. Comparison of the waveforms of Figs. 11 and 12 shows that globally the shapes look similar. However, on a more detailed level there are some differences. The velocity errors of 200 periods, as shown in Fig. 12, are smaller than the velocity errors of the model-based waveforms in Fig. 11. The rms value of the velocity error equals $\mathrm{rms}(e_{v,e}) = 17.01$ μm/s.

D. Discussion

Since the experiments show that the error of the model-based optimization is larger than the data-based optimization, the latter is recommended. Alternatively, the derivation of a model that even more accurately describes the velocity of the stage and piezo legs could further improve the model-based waveform optimization results. This is a subject for future research.

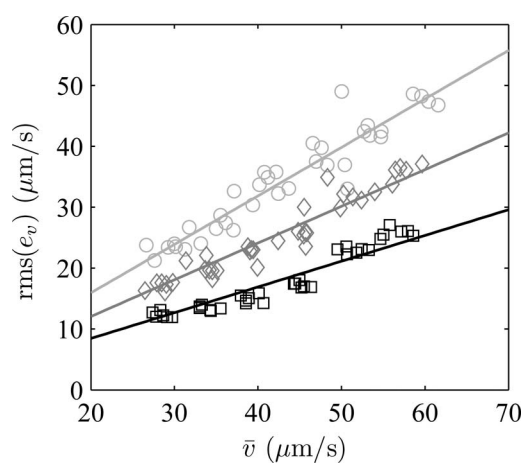

Fig. 13. Velocity errors for experiments with asymmetric waveforms (light gray), model-based optimized waveforms (dark gray) and data-based optimized waveforms (black) for driving frequencies $f_\alpha \in \{10, 12, 14, 16, 18, 20\}$ Hz.

In Fig. 13, the velocity errors of experiments at different driving frequencies $f_\alpha \in \{10, 12, 14, 16, 18, 20\}$ Hz are shown for the asymmetric waveforms of [1], the model-based optimized waveforms, and the data-based waveforms. It can be seen that both optimized waveforms outperform the asymmetric waveforms for all driving frequencies. The best performance is

obtained with the data-based optimized waveforms. A least squares fit through the experimental data is shown in Fig. 13 by the solid lines. For a velocity of 50 μm/s, the model-based waveforms outperform the asymmetric waveforms by 24%. The data-based optimized waveforms reduce the velocity error by 47% compared to the asymmetric waveforms and by 30% compared to the model-based waveforms.

The results shown in this paper are all obtained in open-loop experiments. Using the walking piezo motor with the optimal waveforms in a closed-loop setting [1] is expected to further improve the performance of the nano-motion stage.

By describing each waveform by independent parameters, more freedom is obtained in the optimization to better account for the characteristics of the specific motor, thus improving the results. However, these characteristics might change between motors. So, the optimal waveforms obtained with more independent optimization parameters might not be optimal for a batch of motors.

The optimized waveforms are described by eight parameters, representing points on one period of the waveforms. The Fourier series model (20) through the eight points can exceed the allowable voltage range. If the range is exceeded, linear scaling is applied such that the fitted waveforms do not exceed the allowable range of $u_i \in [0, 46]$ V, $i \in \{1, 2, 3, 4\}$.

Since the used driving frequency and voltage range for the piezo actuator are relatively small, the effect of hysteresis is assumed negligibly small and a linear input–output behavior is assumed. However, although hysteresis is not explicitly taken into account in the model of Section III, the optimized waveforms might still compensate for the hysteresis, since it is present in the experimental data used for the optimization of the waveforms. For higher frequencies, i.e., for rapidly varying reference signals, hysteresis may not be neglected anymore and should be added to the model, which is a subject for future research.

VI. Conclusion

In this paper, a model for a nano-motion stage driven by a walking piezo actuator is presented. The model includes the alternating drive principle of the drive legs of the piezo motor, the contact dynamics between motor and stage and the stick-slip behavior between the legs and the stage. Since the driving principle of the motor depends on friction, it is important that the exact friction force is known at each time instant. Therefore, the friction is modeled using a set-valued force law to accommodate for nonzero friction forces at zero relative velocity. For the resulting model, formulated in terms of a differential inclusion, we developed a dedicated time-stepping solver. Furthermore, the model is used in a waveform optimization, which derives optimal leg orbits to improve the driving properties of the motor. Finally, a data-based waveform optimization was applied to further improve the driving properties of the motor.

The dedicated time-stepping solver is able to simulate the model in terms of a set of differential inclusions. The model is identified using experimental data for different waveforms. The identification and validation experiments show that the model describes the experimental data in the driving x-direction with an accuracy of 93% and in the perpendicular y-direction with an accuracy of 80% for all tested waveforms.

Waveforms are optimized for a constant stage velocity, using a model-based optimization. Compared to the asymmetric waveforms as derived in earlier work [1], the model-based waveforms reduce the velocity error by 24%. The reduction is limited by the accuracy of the velocity as predicted by the model. Therefore, a data-based waveform optimization is performed using direct measurements of the stage position. The data-based optimized waveforms reduce the velocity error by 47% compared to the asymmetric waveforms and by 30% compared to the model-based waveforms.

Future work will include the derivation of a model that more accurately predicts the leg and stage velocities, to further improve the results of the model-based waveform optimization.

References

[1] R. J. E. Merry, N. C. T. De Kleijn, M. J. G. Van de Molengraft, and M. Steinbuch, "Using a walking piezo actuator to drive and control a high precision stage," *IEEE/ASME Trans. Mechatronics*, vol. 14, no. 1, pp. 21–31, Feb. 2009.

[2] R. J. E. Merry, "Performance-driven model-based control for nano-motion systems," Ph.D. dissertation, Eindhoven Univ. Technol., Eindhoven, Netherlands, Nov. 2009, ISBN 978-90-386-2059-6.

[3] E. Elka, D. Elata, and H. Abramovich, "The electromechanical response of multilayered piezoelectric structures," *J. Microelectromech. Syst.*, vol. 13, no. 2, pp. 332–341, 2004.

[4] J. Wallaschek, "Contact mechanics of piezoelectric ultrasonic motors," *Smart Mater. Struct.*, vol. 7, pp. 369–381, 1998.

[5] S. Kim and S. H. Kim, "A precision linear actuator using piezoelectrically driven friction force," *Mechatronics*, vol. 11, no. 8, pp. 969–985, 2001.

[6] J. J. Moreau, *Unilateral Contact and Dry Friction in Finite Freedom Dynamics*. vol. 302 (ser. Non Smooth Mechanics and Applications, CISM Courses and Lectures), New York: Springer-Verlag, 1988.

[7] C. Glocker, *Set-Valued Force Laws, Dynamics of Non-Smooth Systems*. vol. 1 (ser. Lecture Notes in Applied and Computational Mechanics), New York: Springer-Verlag, 2001, ISBN 978-3-540-41436-0.

[8] R. I. Leine and N. Van de Wouw, *Stability and Convergence of Mechanical Systems with Unilateral Constraints,* vol. 36 (ser. Lecture Notes in Applied and Computational Mechanics), New York: Springer-Verlag, 2008, ISBN 978-3-540-76974-3.

[9] V. Acary and B. Brogliato, *Numerical Methods for Nonsmooth Dynamical Systems, Applications in Mechanics and Electronics,* vol. 35 (ser. Lecture Notes in Applied and Computational Mechanics), New York: Springer-Verlag, 2008, ISBN 978-3-540-75391-9.

[10] F. Pfeiffer and C. Glocker, *Multibody Dynamics with Unilateral Contacts*. New York: Wiley, 1996, ISBN 978-0-471-15565-2.

[11] R. I. Leine and H. Nijmeijer, *Dynamics and Bifurcations of Non-Smooth Mechanical Systems,* vol. 18 (ser. Lecture Notes in Applied and Computational Mechanics), New York: Springer-Verlag, 2004, ISBN 978-3-540-21987-3.

[12] N. Petit, M. B. Milam, and R. M. Murray, "Inversion based constrained trajectory optimization," in *Proc. IFAC Symp. Nonlinear Control Syst.*, Jul. 2001, pp. 1–6.

[13] A. J. Fleming and A. G. Wills, "Optimal input signals for bandlimited scanning systems," in *Proc. IFAC World Congr.*, Seoul, Korea, Jul. 2008, pp. 11 805–11 810.

[14] T. Kusakawa, A. Torii, K. Doki, and A. Ueda, "Control waveforms applied to piezo elements used in a miniature robot," in *Proc. Int. Symp. Micro-Nanomechatron. Human Sci.*, Oct. 2004, pp. 307–312.

[15] T. Y. Jiang, T. Y. Ng, and K. Y. Lam, "Optimization of a piezoelectric ceramic actuator," *Sens. Actuators A*, vol. 84, no. 1–2, pp. 81–94, 2000.

[16] J. Lopez-Sanchez, P. Miribel-Catala, E. Montane, M. Puig-Vidal, S. A. Bota, J. Samitier, U. Simu, and S. Johansson, "High accuracy piezoelectric-based microrobot for biomedical applications," in *Proc. IEEE Conf. Emerg. Technol. Factory Autom.*, Oct. 2001, pp. 603–609.

[17] H. V. Brussel, D. Reynaerts, P. Vanherck, M. Versteyhe, and S. Devos, "A nanometre-precision, ultra-stiff piezostepper stage for ELID-grinding," *CIRP Ann.—Manuf. Technol.*, vol. 52, no. 1, pp. 317–322, 2003.

[18] J. H. Holland, *Adaptation in Natural and Artificial Systems: An Introductory Analysis with Applications to Biology, Control, and Artificial Intelligence*. Cambridge, MA: MIT Press, 1992, ISBN 0-262-58111-6.
[19] E. Elbeltagi, T. Hegazy, and D. Grierson, "Comparison among five evolutionary-based optimization algorithms," *Adv. Eng. Inf.*, vol. 19, no. 1, pp. 43–53, 2005.
[20] R. S. Sexton, R. E. Dorsey, and J. D. Johnson, "Optimization of neural networks: A comparative analysis of the genetic algorithm and simulated annealing," *Eur. J. Oper. Res.*, vol. 114, no. 3, pp. 589–601, 1999.
[21] J. Kennedy and R. Eberhart, "Particle swarm optimization," in *Proc. IEEE Int. Conf. Neural Netw.*, Nov. 1995, pp. 1942–1948.
[22] M. Clerc, "The swarm and the queen: Towards a deterministic and adaptive particle swarm optimization," *Congr. Evol. Comput.*, vol. 3, pp. 1951–1957, Jul. 1999.
[23] I. C. Trelea, "The particle swarm optimization algorithm: Convergence analysis and parameter selection," *Inf. Process. Lett.*, vol. 85, no. 6, pp. 317–325, 2003.
[24] P. M. Pardalos and H. E. Romeijn, *Handbook of Global Optimization*. vol. 2, Norwell, MA: Kluwer, 2002, ISBN 1-4020-0632-2.
[25] L. Hamm, B. Brorsen, and M. Hagan, "Comparison of stochastic global optimization methods to estimate neural network weights," *Neural Process. Lett.*, vol. 26, no. 3, pp. 145–158, 2007.
[26] *PiezoLEGS motor*, Piezomotor, AB, 2004. [Online]. Available: www.piezomotor.com
[27] H. J. M. T. S. Adriaens, W. L. D. Koning, and R. Banning, "Modeling piezoelectric actuators," *IEEE/ASME Trans. Mechatronics*, vol. 5, no. 4, pp. 331–341, Dec. 2000.
[28] M. Goldfarb and N. Celanovic, "Modeling piezoelectric stack actuators for control of micromanipulation," *IEEE Control Syst. Mag.*, vol. 17, no. 3, pp. 69–79, Jun. 1997.
[29] S. H. Chang, C. K. Tseng, and H. C. Chien, "An ultra-precision XYθ_z piezo-micropositioner. Part I: Design and analysis," *IEEE Trans. Ultrason., Ferroelectr. Freq. Control*, vol. 46, no. 4, pp. 897–905, Jul. 1999.
[30] A. Preumont, *Mechatronics Dynamics of Electromechanical and Piezoelectric Systems,* vol. 136 (ser. Solid Mechanics and Its Applications), New York: Springer-Verlag, 2006, ISBN 1-4020-4695-2.
[31] B. Bhushan, *Modern Tribology Handbook*. vol. 1, Boca Raton, FL: CRC Press, 2001. ISBN 0-8493-8403-6.
[32] B. N. Norden, "On the compression of a cylinder in contact with a plane surface," Institute for Basic Standards, National Bureau of Standards, Washington, D.C., Tech. Rep. NBSIR 73-243, Jul. 1973.
[33] E. Hairer and G. Wanner, *Solving Ordinary Differential Equations II: Stiff and Differential-Algebraic Problems,* vol. 14 (ser. Springer Series in Computational Mathematics). Berlin, Germany: Springer-Verlag, 2002, ISBN 3-540-60452-9.

Roel J. E. Merry (S'06–M'10) received the M.Sc. degree (*cum laude*) and the Ph.D. degree in mechanical engineering from the Eindhoven University of Technology, Eindhoven, The Netherlands, in 2005 and 2009, respectively. His Ph.D. research focused on the performance-driven control of nano-motion systems.

Since 2005, he has been participating in the RoboCup competition as a member of Tech United Eindhoven, where he was Team Leader from 2007 to 2009. He has been a member of the RoboCup Middle-Size League Executive Committee since 2009. He is currently a Mechatronics Development Engineer at the TMC Group, Eindhoven, The Netherlands. His research interests include the analysis and control of mechatronic systems, especially with piezoelectric actuators.

Martijn G. J. M. Maassen received the M.Sc. degree in mechanical engineering from the Control Systems Technology Group, Department of Mechanical Engineering, Eindhoven University of Technology, Eindhoven, The Netherlands, in 2009.

He is currently a Mechatronics Design Engineer at the TMC Group, Eindhoven, The Netherlands, where he is engaged in research on calibration and integration of stages in a semiconductor machine.

Marinus (René) J. G. van de Molengraft received the M.Sc. degree (*cum laude*) in mechanical engineering and the Ph.D. degree in identification of mechanical systems for control, in 1986 and 1990, respectively, both from Eindhoven University of Technology, Eindhoven, The Netherlands.

From 1986 to 1990, he was a Research Assistant at Eindhoven University of Technology. In 1991, he fulfilled his military service. Since 1992, he has been a Staff Member of the Control Systems Technology Group, Mechanical Engineering Department, Eindhoven University of Technology, where he was an Assistant Professor from 1992 to 2008 and has been an Associate Professor since 2008. In 2005, he founded the Tech United RoboCup Team (vice world champion in 2008 and 2009). His current research interests include real-time control of embedded motion systems and the integrated design of mechatronic systems. He has been an Associate Editor of IFAC *Mechatronics* since 2008.

Nathan van de Wouw (M'09) received the M.Sc. degree with honors (*cum laude*) and the Ph.D. degree in mechanical engineering from the Eindhoven University of Technology, Eindhoven, The Netherlands, in 1994 and 1999, respectively.

Since 1999, he has been affiliated with the Group of Dynamics and Control, Department of Mechanical Engineering, Eindhoven University of Technology, as an Assistant/Associate Professor. In 2000, he was with Philips Applied Technologies, Eindhoven, The Netherlands. In 2001, he was with the Netherlands Organization for Applied Scientific Research, Delft, The Netherlands. From 2006 to 2007, he was a Visiting Professor at the University of California, Santa Barbara, and the University of Melbourne, Australia, from 2009 to 2010. He is the author or coauthor of various papers published in a large number of journal and conference proceedings and the books *Uniform Output Regulation of Nonlinear Systems: A Convergent Dynamics Approach* (Birkhauser, 2005) and *Stability and Convergence of Mechanical Systems with Unilateral Constraints* (Springer-Verlag, 2008). His current research interests include the analysis and control of nonlinear/nonsmooth systems and networked control systems.

Maarten Steinbuch (S'83–M'84–SM'02) received the M.Sc. and Ph.D. degrees from Delft University of Technology, Delft, The Netherlands, in 1984 and 1989, respectively.

From 1987 to 1999, he was with Philips Electronics, Eindhoven. Since 1999, he has been a Full Professor in the Control Systems Technology Group, Mechanical Engineering Department, Eindhoven University of Technology (TU/e), Eindhoven, The Netherlands. His current research interests include modeling, design, and control of motion systems, robotics, automotive powertrains and control for nuclear fusion.

Prof. Steinbuch was an Associate Editor of the IEEE TRANSACTIONS ON CONTROL SYSTEMS TECHNOLOGY, the International Federation of Automatic Control (IFAC) *Journal of Control Engineering Practice*, and the IEEE CONTROL SYSTEMS MAGAZINE. He was an Editor-at-Large of the *European Journal of Control*, Editor-in-Chief of IFAC *Journal of the Mechatronics*, and Associate Editor of the *International Journal of Powertrains*. He is a Program Leader of the TU/e Master of Science Automotive Technology. Since July 2006, he has also been the Scientific Director of the Center of Competence High Tech Systems of the Federation of Dutch Technical Universities. In 2003, 2005, and 2008, he received the Best-Teacher award from the Department of Mechanical Engineering, TU/e.